Supplementary Information

# Energy-based modeling of micro- and nano-droplet jumping upon coalescence on superhydrophobic surfaces

**Jun-Jie Huang**[1,2*], **Haibo Huang**[3], **Jian-Jun Xu**[4]

[1] Department of Engineering Mechanics, College of Aerospace Engineering, Chongqing University, Chongqing 400044, China

[2] Chongqing Key Laboratory of Heterogeneous Material Mechanics (Chongqing University), Chongqing 400044, China

[3] Department of Modern Mechanics, University of Science and Technology of China, Hefei, Anhui 230026, China

[4] Chongqing Institute of Green and Intelligent Technology, Chinese Academy of Sciences, Chongqing, 400714, China

September 13, 2019

## S1 Phase-Field Lattice-Boltzmann Simulation Method

The present numerical results on the coalescence of two droplets were obtained by using a phase-field-based hybrid lattice-Boltzmann finite-difference method [7]. The interface dynamics is described by the Cahn-Hilliard equation (CHE) which is solved by the finite-difference method, and the hydrodynamics is simulated by the lattice-Boltzmann method (LBM) [2, 10]. Some basic components of the method are given below.

*Corresponding author. E-mail: jjhuang1980@gmail.com; jjhuang@cqu.edu.cn.

The free energy functional $\mathcal{F}$ for binary fluids is,

$$\mathcal{F}(\phi, \boldsymbol{\nabla}\phi) = \int_V \left( \Psi(\phi) + \frac{1}{2}\kappa |\boldsymbol{\nabla}\phi|^2 \right) dV, \tag{S1.1}$$

where $\Psi(\phi) = a(\phi^2 - 1)^2$ is the bulk free energy density and $\frac{1}{2}\kappa|\boldsymbol{\nabla}\phi|^2$ is the interfacial energy density. The two constants $a$ and $\kappa$ are computed from the interfacial tension $\sigma$ and interface thickness $W$ as,

$$a = \frac{3\sigma}{4W},\ \kappa = \frac{3\sigma W}{8}. \tag{S1.2}$$

The order parameter $\phi$ varies between 1 in the liquid and $-1$ in the gas. The chemical potential $\mu$ is,

$$\mu = \frac{\delta \mathcal{F}}{\delta \phi} = \frac{d\Psi(\phi)}{d\phi} - \kappa \nabla^2 \phi = 4a\phi(\phi^2 - 1) - \kappa \nabla^2 \phi. \tag{S1.3}$$

The CHE with convection and a constant mobility $M$ can be written as [8],

$$\frac{\partial \phi}{\partial t} + \boldsymbol{u} \cdot \boldsymbol{\nabla}\phi = M \nabla^2 \mu, \tag{S1.4}$$

where $\boldsymbol{u}$ is the fluid velocity. The phase-field equations, (S1.3) and (S1.4), are discretized in space by the $2^{nd}-$order finite-difference method and integrated in time by the $4^{th}-$order Runge-Kutta method [6]. The grid size is $\delta_x$ and time step is $\delta_t$. For two-phase flows, the force due to interfacial tension may be written as $\boldsymbol{F}_s = \mu \boldsymbol{\nabla}\phi$.

When the single-relaxation-time collision model is used, the lattice-Boltzmann equations (LBEs) for hydrodynamics read [10],

$$f_i(\boldsymbol{x} + \boldsymbol{e}_i\delta_t, t + \delta_t) - f_i(\boldsymbol{x}, t) = -\frac{1}{\tau_f}(f_i - f_i^{eq}) + \left(1 - \frac{1}{2\tau_f}\right)(\boldsymbol{e}_i - \boldsymbol{u}) \cdot [\boldsymbol{\nabla}\rho c_s^2(\Gamma_i - \Gamma_i(0)) + \boldsymbol{F}_s\Gamma_i], \tag{S1.5}$$

where $f_i$ and $f_i^{eq}$ are the distribution functions (DFs) and equilibrium DFs along the direction of the lattice velocity $\boldsymbol{e}_i$ $(i = 0, 1, \cdots, b)$, $c_s$ is the lattice sound speed (the lattice velocity $c = \delta_x/\delta_t = \sqrt{3}c_s$ for the D3Q19 velocity model used here), and $\tau_f$ is the relaxation parameter. For D3Q19, the lattice velocity (vector) $\boldsymbol{e}_i$ reads,

$$\boldsymbol{e}_i = (e_{ix}, e_{iy}, e_{iz}) = \begin{cases} (0,0,0) & \text{for } i = 0 \\ (\pm 1, 0, 0)c;\ (0, \pm 1, 0)c;\ (0, 0, \pm 1)c; & \text{for } i = 1 - 6 \\ (\pm 1, \pm 1, 0)c;\ (\pm 1, 0, \pm 1)c;\ (0, \pm 1, \pm 1)c; & \text{for } i = 7 - 10; 11 - 14; 15 - 18 \end{cases}. \tag{S1.6}$$

The density $\rho$ and kinematic viscosity $\nu$ of the fluid depends on the order parameter $\phi$ as,

$$\rho(\phi) = \frac{\phi+1}{2}\rho_L + \frac{1-\phi}{2}\rho_G, \ \frac{1}{\nu(\phi)} = \frac{\phi+1}{2}\frac{1}{\nu_L} + \frac{1-\phi}{2}\frac{1}{\nu_G}, \tag{S1.7}$$

where $\rho_L$ and $\rho_G$ are the densities of the liquid and gas, and $\nu_L$ and $\nu_G$ are their kinematic viscosities. The dynamic viscosity is $\eta(\phi) = \rho(\phi)\nu(\phi)$. The dynamic viscosities of the liquid and gas are $\eta_L = \rho_L\nu_L$ and $\eta_G = \rho_G\nu_G$. The relaxation parameter $\tau_f$ is determined from $\nu$ as $\nu = c_s^2(\tau_f - 0.5)\delta_t$. The equilibrium DFs are given by,

$$f_i^{eq} = w_i\left[p + \rho c_s^2\left(\frac{1}{c_s^2}e_{i\alpha}u_\alpha + \frac{1}{2c_s^4}(e_{i\alpha}e_{i\beta} - c_s^2\delta_{\alpha\beta})u_\alpha u_\beta\right)\right], \tag{S1.8}$$

where $w_i$ is the weight for the direction along $\boldsymbol{e}_i$ and $p$ is the hydrodynamic pressure. For D3Q19 $w_i$ is,

$$w_i = \begin{cases} \frac{1}{3} & \text{for } i = 0 \\ \frac{1}{18} & \text{for } i = 1-6 \\ \frac{1}{36} & \text{for } i = 7-18 \end{cases}. \tag{S1.9}$$

$\Gamma_i$ in Eq. (S1.5) is given by $\Gamma_i(\boldsymbol{u}) = w_i[1 + \frac{1}{c_s^2}e_{i\alpha}u_\alpha + \frac{1}{2c_s^4}(e_{i\alpha}e_{i\beta} - c_s^2\delta_{\alpha\beta})u_\alpha u_\beta]$ and $\Gamma_i(0) = w_i$. The pressure and fluid momentum are computed from,

$$p = \sum_i f_i + \frac{1}{2}\delta_t(\boldsymbol{u}\cdot\boldsymbol{\nabla}\rho c_s^2), \tag{S1.10}$$

$$\rho\boldsymbol{u} = \frac{1}{c_s^2}\sum_i f_i\boldsymbol{e}_i + \frac{1}{2}\delta_t\boldsymbol{F}_s, \tag{S1.11}$$

and the fluid velocity is found from Eq. (S1.11) once the density $\rho(\phi)$ is known from $\phi$. Through the Chapman-Enskog analysis, it can be found that the LBEs, Eq. (S1.5), approximate the following equations at the macroscopic level [11],

$$\frac{\partial p}{\partial t} + \rho c_s^2\boldsymbol{\nabla}\cdot\boldsymbol{u} = 0, \tag{S1.12}$$

$$\rho\left(\frac{\partial\boldsymbol{u}}{\partial t} + \boldsymbol{u}\cdot\boldsymbol{\nabla}\boldsymbol{u}\right) = -\boldsymbol{\nabla}p + \boldsymbol{F}_s + \boldsymbol{\nabla}\cdot\boldsymbol{\Pi}, \tag{S1.13}$$

where $\boldsymbol{\Pi} = \eta(\phi)[\boldsymbol{\nabla}\boldsymbol{u} + (\boldsymbol{\nabla}\boldsymbol{u})^T]$ is the viscous stress tensor for incompressible Newtonian fluids. To improve stability, we used the weighted multiple-relaxation-time (MRT) collision model [4] which contains further improvement as compared with the original MRT model in [9].

## S2 Numerical Results on Droplet Coalescence

Initially, there are two stationary droplets having the same radius $R$ on the $x-$axis. Their initial centers are located at $(x_d, y_d, z_d) = (\pm R, 0, 0)$. The problem is symmetric about the $x-$axis and the $y-z$ plane. One eighth of the domain is used for all simulations (see fig. S1). On all boundaries, symmetric boundary conditions are applied. The liquid density $\rho_L$ is taken as the reference density. The initial radius $R$ is chosen as the reference length $L_r$. The domain size is $L_x \times L_y \times L_z = 3 \times 3 \times 3$. The capillary-inertial velocity $U_{ci} = \sqrt{\sigma/(\rho_L R)}$ is chosen as the reference velocity $U_r$. From $L_r$ and $U_r$, a reference time is derived as $T_r = L_r/U_r = R/U_{ci} = \sqrt{\rho_L R^3/\sigma}$. All lengths, velocities and times are scaled by $L_r$, $U_r$ and $T_r$ respectively. In our simulations, the reference length $L_r$ is discretized into $N_L$ uniform segments and the reference time $T_r$ is discretized into $N_t$ uniform intervals. The grid size and time step are $\delta_x = L_r/N_L$ and $\delta_t = T_r/N_t$. In phase-field simulations, there are two numerical parameters: the Cahn number $Cn = W/L_r$ (the ratio of interface thickness over the reference length) and the Peclet number $Pe = (U_r L_r^2)/(M\sigma)$ (the ratio of convection over diffusion in the CHE). In order to approach the sharp interface limit (SIL) [8, 22], one should make $Cn(= W/L_r = (W/\delta_x)/N_L)$ as small as possible. With a given $N_L$, a smaller $W/\delta_x$ is preferred. But when $W/\delta_x$ is too small, the profile of $\phi$ across an interface cannot be accurately resolved [8]. For a given $W/\delta_x$, a larger $N_L$ is preferred, but the computation cost increases quickly as $N_L$ becomes larger. We chose $W/\delta_x = 4.0$ to reconcile the above two contradicting requirements [7]. Noted that the Cahn number defined in [22] $Cn_1$ is related to the present one as $Cn_1 = Cn/(2\sqrt{2})$.

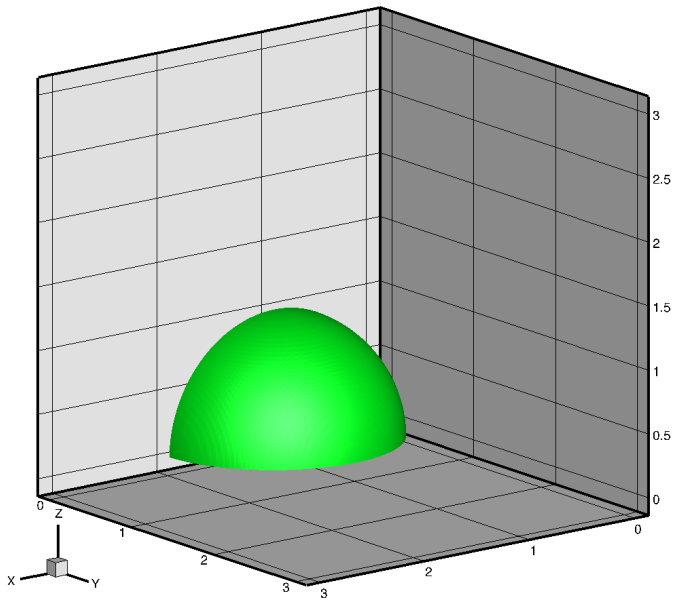


Figure S1: Initial setup for the coalescence of two droplets with the same radius. The box represents one eighth of the whole domain with $x > 0$, $y > 0$ and $z > 0$.

## S2.1 Quantities of interest and numerical validation

The following quantities were monitored during the simulation: the (half) lengths of the coalesced droplet on the $x-$, $y-$ and $z-$axes, $R_x$, $R_y$, and $R_z$, the kinetic energy of the droplet $E_k$ and the total kinetic energy $E_{k,t}$, the surface energy $E_s$, the viscous dissipation rate $R_v$ and the dissipation rate due to the diffusion in the CHE $R_d$. The energies and dissipation rates are calculated as [13, 15, 19],

$$E_k = \int_V N(\phi)\frac{1}{2}\rho_L(u^2+v^2+w^2)dxdydz, \quad E_{k,t} = \int_V \frac{1}{2}\rho(\phi)(u^2+v^2+w^2)dxdydz, \tag{S2.1}$$

$$E_s = \int_V \left[a(\phi^2-1)^2 + \frac{1}{2}\kappa|\boldsymbol{\nabla}\phi|^2\right]dxdydz, \tag{S2.2}$$

$$\begin{aligned} R_{vis} = \int_V 2\eta(\phi)\Bigg\{&\left(\frac{\partial u}{\partial x}\right)^2 + \left(\frac{\partial v}{\partial y}\right)^2 + \left(\frac{\partial w}{\partial z}\right)^2 \\ &+ \frac{1}{2}\left[\left(\frac{\partial u}{\partial y}+\frac{\partial v}{\partial x}\right)^2 + \left(\frac{\partial u}{\partial z}+\frac{\partial w}{\partial x}\right)^2 + \left(\frac{\partial v}{\partial z}+\frac{\partial w}{\partial y}\right)^2\right]\Bigg\}dxdydz, \end{aligned} \tag{S2.3}$$

$$R_d = \int_V \frac{1}{M}\left[\left(\frac{\partial \mu}{\partial x}\right)^2 + \left(\frac{\partial \mu}{\partial y}\right)^2 + \left(\frac{\partial \mu}{\partial z}\right)^2\right]dxdydz, \tag{S2.4}$$

where the integrations are carried out over the whole domain, $u$, $v$ and $w$ are the velocity components in the $x-$, $y-$ and $z-$directions, and the function $N(\phi)$ is 1 when $\phi > 0$ and 0 otherwise. The viscous dissipation $E_{vis}$ and the dissipation due to the CHE diffusion $E_d$ can be found from $R_v$ and $R_d$ as $E_{vis} = \int_0^t R_{vis}d\tau$ and $E_d = \int_0^t R_d d\tau$ . The total energy is obtained as $E_{total} = E_{k,t} + E_s + E_{vis} + E_d$.

First, the convergence of the results is studied focusing on the evolution of $R_y$ simulated by using different grid sizes and Cahn numbers. A typical case at $Oh = 0.1$ was computed with three sets of numerical parameters given in Table S1. It is noted that if one uses another reference velocity $\sigma/\eta_L$ (derived from the surface tension and the dynamic viscosity of the liquid), all factors related to $Oh$ in the third and fifth columns of Table S1 on $N_t$ and $Pe$ can be eliminated. For reference, the values of $Cn_1$ are also given in Table S1. Figure S2 shows the evolutions of $R_y$ obtained for the three sets. It is seen that the differences between the three sets are in general not large and the change in $R_y$ as $Cn$ is reduced from 0.1 to 0.0714 is smaller than that when $Cn$ is reduced from 0.14286 to 0.1. Since the simulation is much more time consuming at $Cn = 0.0714$ than at $Cn = 0.1$, we used $Cn = 0.1$ in most simulations. Note that $N_t$ was varied for different $Oh$ to ensure that the relaxation parameter $\tau_f$ remains in a suitable range.

Table S1: Numerical parameters for the simulation of a typical case of droplet coalescence.

| Set No. | $N_L$ | $N_t$ | $Cn$ ($Cn_1$) | $Pe$ |
|---|---|---|---|---|
| 1 | 28 | $280/Oh$ | 0.14286 (0.051) | $8000Oh$ |
| 2 | 40 | $400/Oh$ | 0.1 (0.035) | $8000Oh$ |
| 3 | 56 | $840/Oh$ | 0.0714 (0.025) | $8000Oh$ |

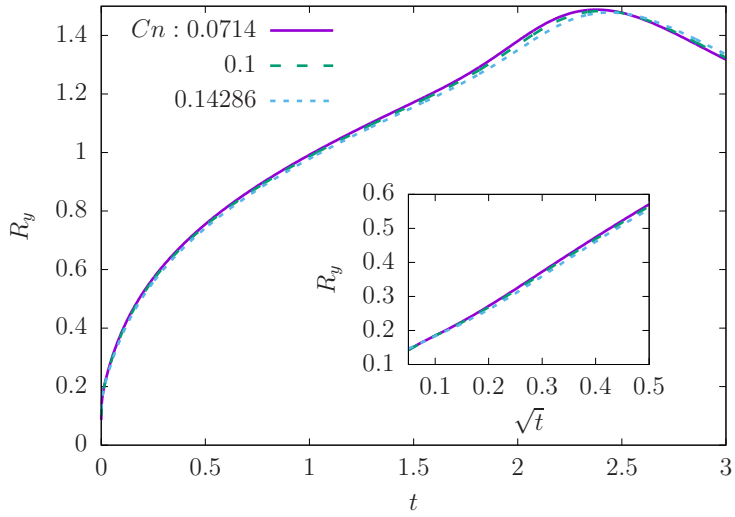


Figure S2: Evolution of the (half) length of the droplet on the $y-$axis $R_y$ at $Oh = 0.1$ under three different sets of numerical parameters. The inset shows the variation of $R_y$ with $\sqrt{t}$ for $t \leq 0.25$.

Next, the evolutions of $R_x$ and $R_y$ are studied ($R_z$ is not plotted as $R_z = R_y$ throughout the simulations). Figure S3 shows their evolutions at $Oh = 0.4$, 0.1 and 0.037 obtained with $Cn = 0.1$. It is found that $R_x$ and $R_y$ show more oscillations at $Oh = 0.037$ because the capillary-inertial effect is more significant. In contrast, they vary more smoothly at $Oh = 0.4$ due to the large viscous effect. As $Oh$ increases, the time to reach the pseudo equilibrium state is extended. It is also seen that for the three cases the time to reach the pseudo equilibrium state almost matches the time for $R_y$ to reach its equilibrium value $2^{\frac{1}{3}} \approx 1.2599$. Note that we determine the first pseudo equilibrium state as the moment when the length of the coalesced droplet in the $x-$direction is equal to those in the $y-$ and $z-$directions. This criterion differs from that in [3] (they used the time when the neck radius reaches its equilibrium value $2^{\frac{1}{3}}$). We found that the results by using these two criteria are close for most cases when $Oh$ is not very small (the SI of [3] also supports this observation).

To validate the present simulations the coalescence time was examined for droplets of different sizes. Following [1], we define the coalescence time $t_{coal}$ to be the time when the neck radius of the coalesced droplet ($R_y$) is equal to the initial radius $R$. Figure S4 shows the variation of $t_{coal}$ with $R$ by the present simulations and also the data from the experiments in [1]. When the coalescence is dominated by CI effects, the coalescence time is predicted by $\tau_{inv} = \frac{1}{D_0^2}\sqrt{\frac{\rho_L R^3}{\sigma}}$ with the constant $D_0$ varying between 1.39 and 1.62 whereas in the viscous regime it is predicted by $\tau_{vis} = R\eta_L/\sigma$ [1]. The predictions by $\tau_{inv}$ and $\tau_{vis}$ are also given in fig. S4. It is seen that the present results follow $\tau_{inv}$ with $D_0 = 1.39$ more closely and also agree with the measurements in [1]. As the droplet radius decreases, the coalescence time seems to become larger than $\tau_{inv}$ more. Similar trend can be observed in the experiment data from [1].

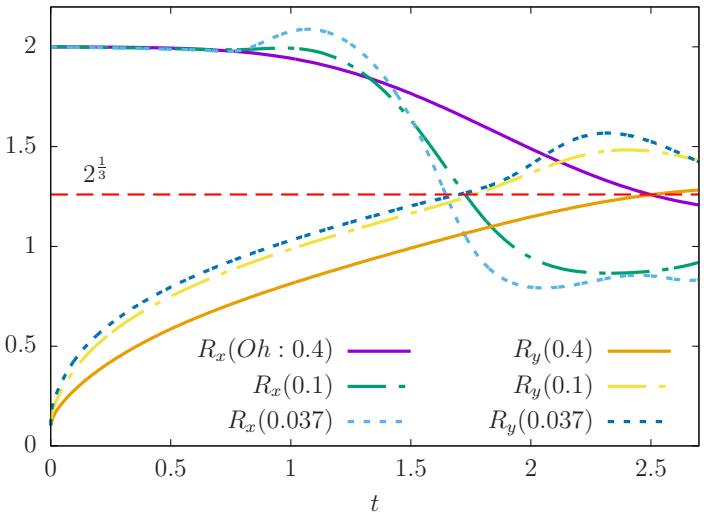


Figure S3: Evolution of the (half) lengths of the droplet on the $x-$ and $y-$ axes, $R_x$ and $R_y$, at $Oh = 0.4$, 0.1 and 0.037. The numerical parameters are from Set 2 in Table S1. The horizontal line shows the final equilibrium radius of the coalesced droplet.

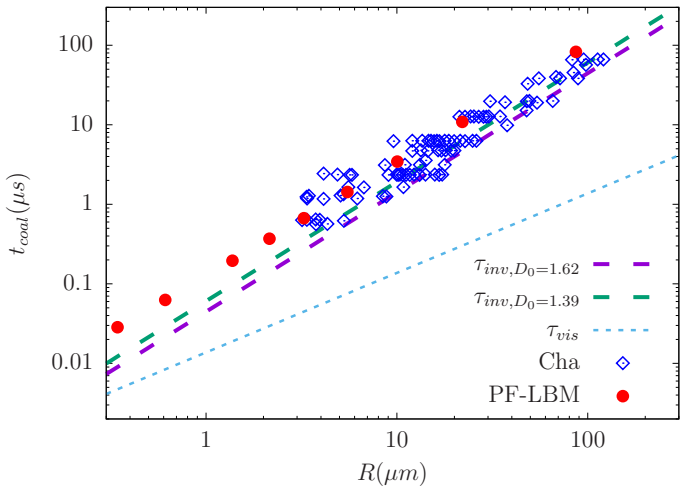


Figure S4: Variation of the coalescence time with the initial droplet radius. The empty diamonds are from the experimental measurements in [1].

### S2.2 Examination of various energies and forms of energy dissipation

Finally, we examine how various energies change during the droplet coalescence process. Figure S5 shows the evolutions of $E_k/E_{total}$, $E_{k,t}/E_{total}$, $E_s/E_{total}$, $E_{vis}/E_{total}$, $E_d/E_{total}$ and $E_{total}/E_{total}(0)$ at $Oh = 0.4$, 0.1 and 0.037. At the beginning, the total energy is equal to the surface energy, i.e., $E_{total}(0) = E_s(0)$. From fig. S5, some common characteristics are observed for all three cases: (1) the total energy remains nearly constant during the simulation; (2) the total kinetic energy is almost equal to the droplet's kinetic energy (attributable to the relatively large density and viscosity ratios); (3) in the pseudo equilibrium state the surface energy (scaled by $E_{total} \approx E_s(0)$) reduces to its minimum value close to the theoretical one $2^{-\frac{1}{3}}$ (when the coalesced droplet reaches static equilibrium). The reduction of surface energy is partly converted to the kinetic energy, largely dissipated by the viscous effects, and to some extent, dissipated by the phase-field diffusion. Ideally, the last part $E_d$ should be zero, but it is difficult to completely eliminate the numerical artifacts in phase-field simulations using a finite interface thickness. Comparison with the results in [3] (obtained by using sharp interface simulations free from such artifacts) indicates that the calculation of energy dissipation can be improved by taking $E_d$ into account (see fig. S6a). To better appreciate the dependence of the dissipation energy on the $Oh$ number, it is helpful to examine the derivative of the energy dissipation with respect to $Oh$. Figure S6b compares the derivative for the two power law forms obtained by the present work with the two linear forms. It is seen that in contrast to the linear forms (which give constant derivative: $72\pi$ based on [18] and $3\pi$ according to [14]), the power law forms predict that the derivative decreases as $Oh$ increases. That means, with the same increment in $Oh$, the dissipation energy (scaled by the reference energy $\sigma R^2$) increases more for low $Oh$ (e.g., $Oh$ increases from 0.01 to 0.02) than for high $Oh$ (e.g., $Oh$ increases from 0.1 to 0.11). On the contrary, the linear forms would predict that the increments of the (scaled) dissipation energy are the same for the above two changes at $Oh = 0.01$ and 0.1. The power law form may better reflect the effects of viscosity for different regimes of $Oh$.

## S3 Results on the Coalescence-Induced Droplet Jumping on a Non-wetting Surface

The initial setup for the coalescence-induced droplet jumping on a nonwetting surface is similar to the above for droplet coalescence except that the initial centers of the two droplets are at $(\pm R, 0, R)$ and a nonwetting wall is added at $z = 0$. The problem is symmetric about the $y - z$ plane and the $x - z$ plane. One fourth of the domain is used for all simulations in this section. Stationary wall boundary conditions are applied on the back and front boundaries ($z = 0,\ L_z$) whereas symmetric boundary conditions are applied on all other boundaries.

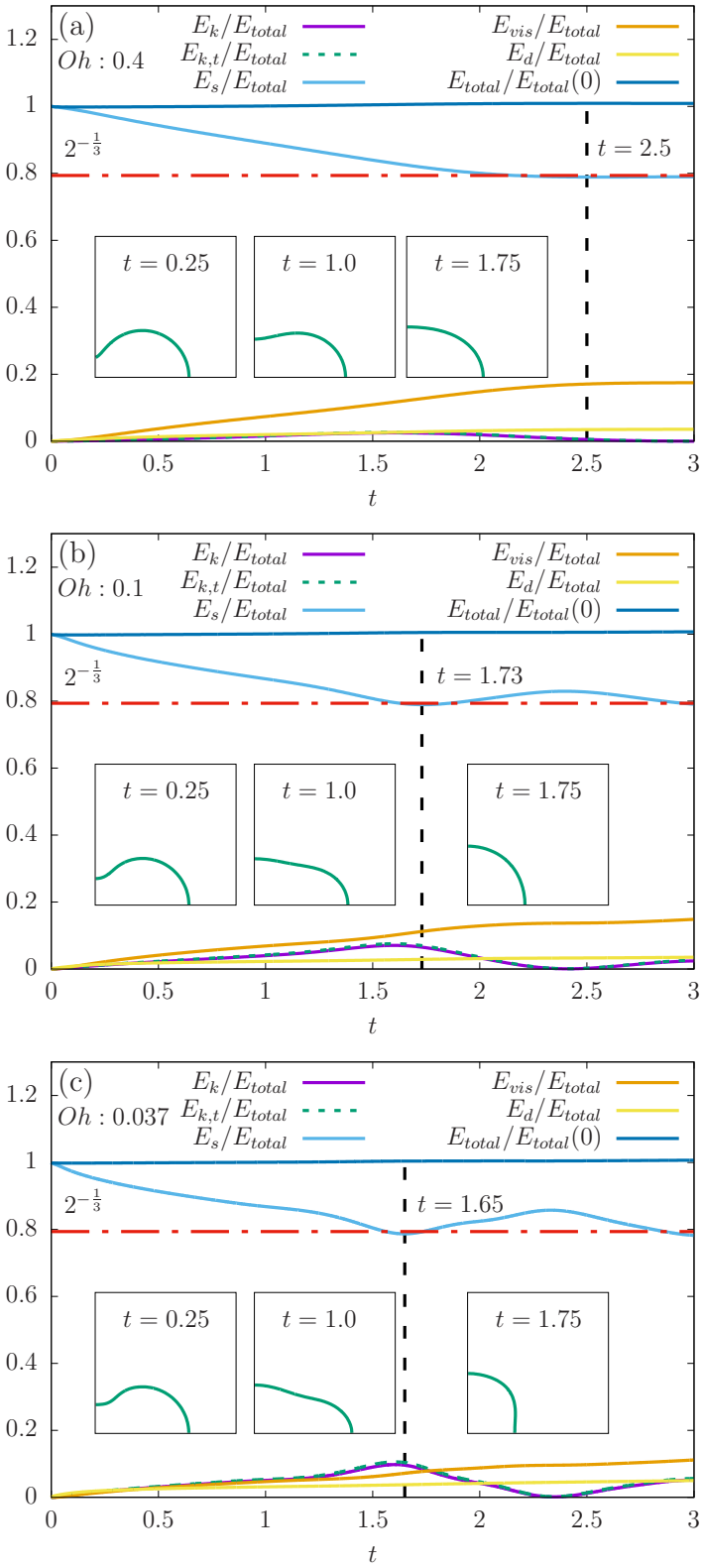


Figure S5: Evolutions of the (scaled) energies for (a) $Oh = 0.4$ (b) $Oh = 0.1$ and (c) $Oh = 0.037$ obtained with $Cn = 0.1$. The vertical dashed line shows the time when the pseudo equilibrium state ($R_x = R_y = R_z$) is achieved. The horizontal dashed line indicates the theoretical value of the (scaled) minimum surface energy $2^{-\frac{1}{3}} \approx 0.7937$. The insets show three snapshots of the interface in the $x - y$ plane at $z = 0$ at $t = 0.25$, 1.0 and 1.75.

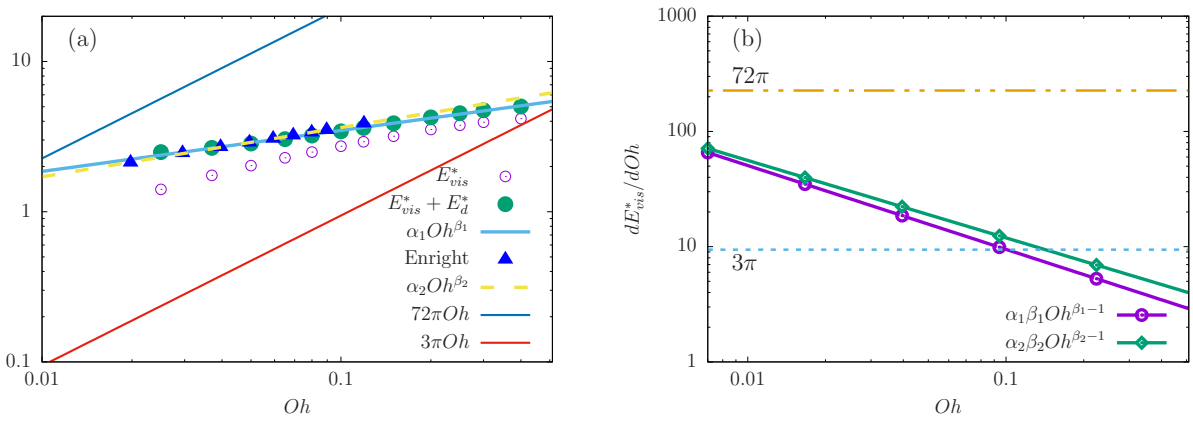


Figure S6: Variation of (a) the energy dissipation with the $Oh$ number (b) the derivative $dE^*_{vis}/dOh$ ($d(E^*_{vis}+E^*_d)/dOh$ for the present data) with the $Oh$ number for the linear forms and power law forms. The empty circles in (a) denote the data for viscous dissipation only by the present simulations.

The reference quantities and numerical parameters are the same as those in the above section except that the domain size is $L_x \times L_y \times L_z = 3 \times 3 \times 5$. The following $Oh$ numbers were considered: $Oh = 0.037$, 0.05, 0.065, 0.08, 0.1, 0.119, 0.15, 0.2, 0.25, 0.3 and 0.4. In addition to those quantities monitored in Section S2, the mass center velocity of the droplet and its translational kinetic energy along the $z-$direction, $w_{cm}$ and $E_{k,tr}$, were also calculated,

$$w_{cm} = \frac{\int_V N(\phi)\rho_L w dxdydz}{\int_V N(\phi)\rho_L dxdydz}, \quad E_{k,tr} = \frac{1}{2}\rho_L w_{cm}^2 \int_V N(\phi) dxdydz. \tag{S3.1}$$

## S3.1 Results for typical cases

Figure S7 shows several snapshots of the interfaces in the $x-z$ plane at $y = 0.5\delta_x$ and in the $y-z$ plane at $x = 0.5\delta_x$ for a typical case at $Oh = 0.1$. The time for droplet jumping $t_{jump}$ is extracted from the interfaces in the two planes. To take into account the diffuse nature of the interfaces in phase field simulations, we used the time when the lowest interface in stage (iii) is $W/2$ above the wall (other choices may cause small differences in the extracted results). Based on this criterion, $t_{jump}$ is estimated to be about 3.25 for this case at $Oh = 0.1$. Figure S8 shows the evolutions of the droplet velocity $w_{cm}$ for three typical cases at $Oh = 0.037$, 0.119 and 0.3. According to [5, 13], the evolution of $w_{cm}$ may be divided into four distinct stages characterized by the following events: (i) the liquid bridge grows; (ii) the coalesced droplet is accelerated toward its maximum velocity; (iii) the coalesced droplet jumps off the wall; (iv) the coalesced droplet velocity is reduced by the air viscosity. As seen in fig. S8, these four stages are easily observed for $Oh = 0.037$. But stages (iii) and (iv) are not easy to be differentiated as $Oh$ increases. This is similar to that reported in [13].

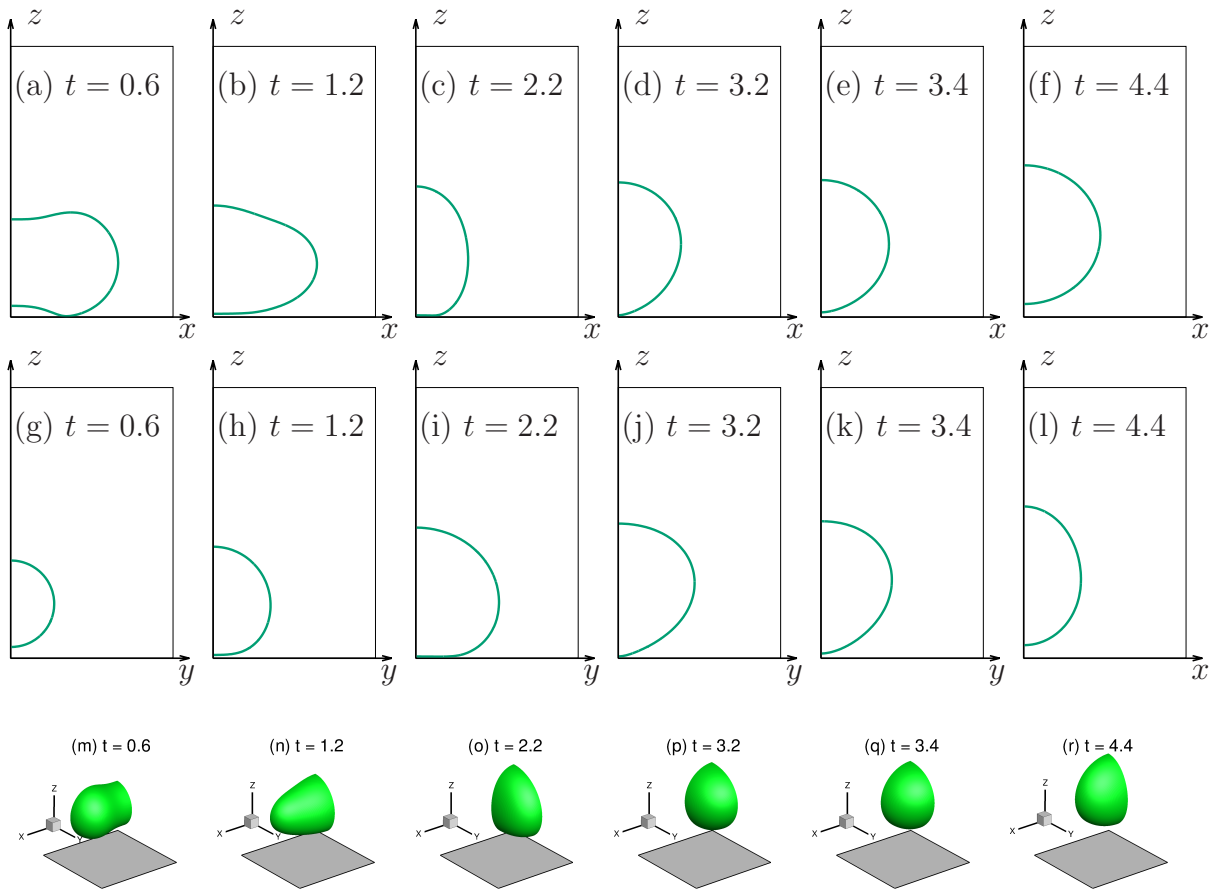


Figure S7: Snapshots of the interfaces in the $x - z$ plane at $y = 0.5\delta_x$ (a-f), in the $y - z$ plane at $x = 0.5\delta_x$ (g-l) and the corresponding 3-D views (m-r) for the coalescence-induced droplet jumping on a nonwetting wall at $Oh = 0.1$. The common parameters are $r_\rho = 50$, $r_\eta = 58.8$, and $\theta_w = 180°$.

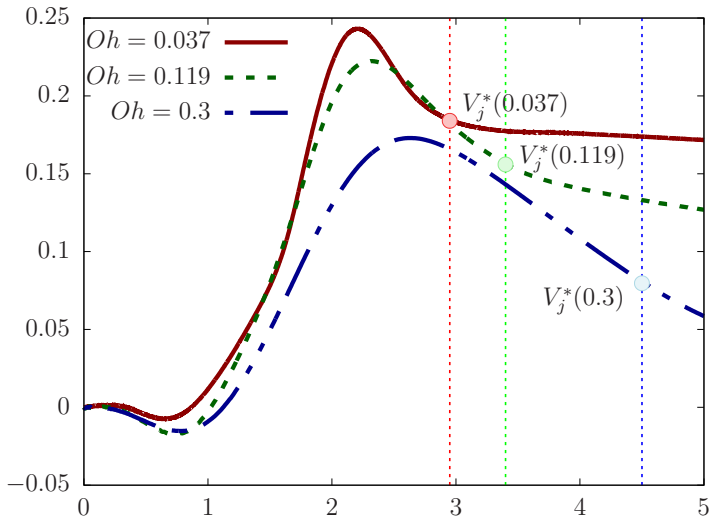


Figure S8: Evolution of the mass center velocity of the droplet along the $z-$direction at three different $Oh$ numbers. The common parameters are $r_\rho = 50$, $r_\eta = 58.8$, and $\theta_w = 180°$. The three vertical dashed lines indicate the times for the droplet jumping $t_{jump}$ for the three cases (from left to right are $Oh = 0.037$, 0.119 and 0.3).

## S3.2 On the energy dissipation

From the simulations of droplet coalescence near a nonwetting wall, we extracted the dissipation energy (containing both the parts related to the fluid viscosity and the CHE diffusion, $E_{vis}$ and $E_d$, as done for the droplet coalescence problem) at the time when the droplet jumps off the surface ($t_{jump}$), denoted by $E_{vis,jump}$ (the $E_{vis}+E_d$ at $t_{eq1}$ in the droplet coalescence problem in Section S2 is now denoted by $E_{vis,eq1}$). At $Oh=0.037$, $E^*_{vis,jump}$ is about 43.7% larger than $E^*_{vis,eq1}$ while at $Oh=0.4$, $E^*_{vis,jump}$ is only about 9% larger. Figure S9 shows the evolutions of the dissipation energy at $Oh=0.037$ and 0.3. It can be observed that at a low $Oh$ the presence of the wall has little effect on the energy dissipation and $E^*_{vis,jump}$ is larger than $E^*_{vis,eq1}$ due to the additional dissipation accumulated between $t_{eq1}$ and $t_{jump}$. In contrast, at a high $Oh$, the effect of the wall (though nonwetting) is more noticeable after the initial coalescence stage. The wall seems to slow down the dissipation to some extent: at $t_{eq1}$ the dissipation when the wall is present is smaller than that without any wall ($E^*_{vis,eq1,nw} < E^*_{vis,eq1}$, see fig. S9b). The reason could be that the wall suppresses the flow inside the droplet (after the coalesced droplet touches the wall) more significantly at a high $Oh$. But the dissipation at the jumping time $E^*_{vis,jump}$ is still larger than $E^*_{vis,eq1}$, although the difference between them is reduced at large $Oh$.

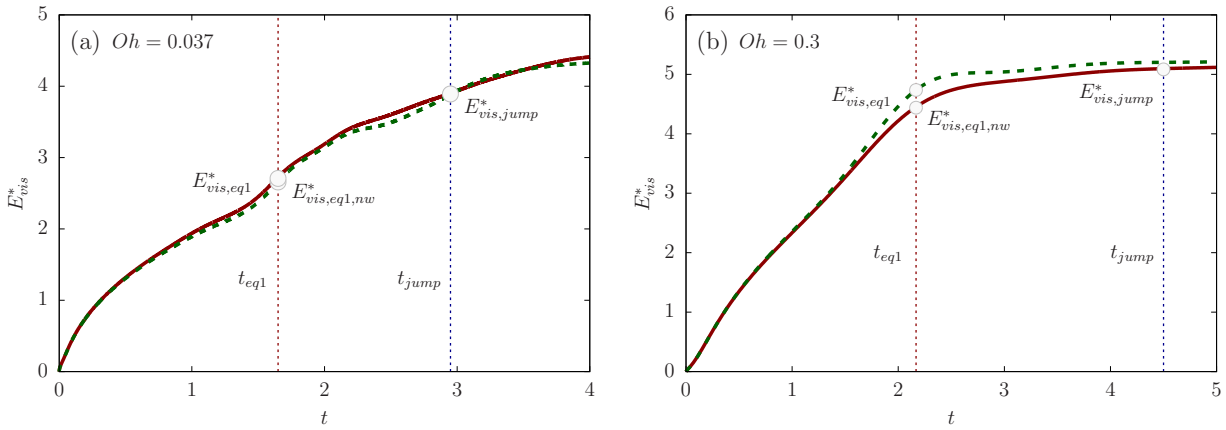


Figure S9: Evolutions of the energy dissipation $E^*_{vis}$ at (a) $Oh=0.037$ and (b) $Oh=0.3$ for the coalescence of two droplets. The solid lines are for the droplet coalescence on a nonwetting wall and the dashed lines are for the free droplet coalescence without any wall.

As mentioned in the main text, the fitting function $f(Oh)$ for $E^*_{vis,jump}$ is multiplied by an coefficient 1.015 before it is used in the model to compensate for the inaccuracy due to numerical errors. The value 1.015 is slightly larger than unity and it is chosen such that the predicted critical $Oh$ number $Oh_c$ is near 0.434. The reasons are as follows. It can be found that $f(0.43)\approx 5.110$ and $f(Oh\to\infty)=5.112$, which is about 99% of the theoretically released surface energy $\Delta E^*_s \approx 5.185$. Although the difference is quite small, the model would predict that the droplet jumps off the nonwetting surface at all $Oh$ numbers if the obtained formula $f(Oh)$ for $E^*_{vis,jump}$ is directly used in the model because the critical $Oh$ number $Oh_c$ is obtained at $f(Oh)/\Delta E^*_s = 1$

which is not realizable by $f(Oh)$. On the other hand, one may estimate $Oh_c$ based on the fitting function for $E^*_{vis,eq1}$. Since $E^*_{vis,jump}$ becomes closer and closer to $E^*_{vis,eq1}$ as $Oh$ increases, it is reasonable to assume that eventually they would become equal at $Oh_c$. From the fitting function $\alpha_1 Oh^{\beta_1}$ for the present data on $E^*_{vis,eq1}$, one finds that $Oh_c \approx 0.434$. In our simulations, the droplet did not jump off the surface at $Oh = 0.45$ whereas droplet jumping occurred at $Oh = 0.4$ with a relatively small jumping velocity. Thus, the above estimation of $Oh_c$ is also consistent with our simulations.

### S3.3 On the portion of translational kinetic energy

Besides the energy dissipation, we also extracted the values of $1/(n+1)$ (i.e., the portion of the translational kinetic energy in the total kinetic energy of the droplet $E_{k,tr}/E_k = E_{k,tr}/(E_{k,tr} + E_{k,os}) = 1/(n+1)$) at $t_{jump}$ when the coalesced droplet jumps off the surface for different $Oh$ numbers. Figure S10 shows the evolutions of $E_{k,tr}/E_k$ at three typical $Oh$ numbers (0.037, 0.119 and 0.3). It is seen that for all three $Oh$ numbers there exist two peaks for $1/(n+1)$ when $t < 5$ and the droplet jumping occurs in between them. As $Oh$ increases, the ratio $1/(n+1)$ increases. Figure S11 shows the evolutions of the oscillatory kinetic energy at $Oh = 0.037$, 0.119 and 0.3. It can be easily observed that $E^*_{k,os}$ is much more quickly damped at $Oh = 0.3$ than at $Oh = 0.037$. When $Oh$ is large enough, the droplet's kinetic energy almost only consists of the translational part at $t_{jump}$.

Due to the inaccuracy in our data and fitting process, the fitting function for $1/(n+1)$, $g(Oh)$, may become marginally larger than unity for large $Oh$ (e.g., $g(Oh_c) = g(0.434) \approx 1.0006$). But unlike the situation for energy dissipation, this small error would not cause significant deviations in the predicted jumping velocity, thus it is directly used in the model. The variation of $g(Oh)$ with $Oh$ can be explained as follows. As the dynamic viscosity ratio is large ($r_\eta = 58.8$), viscous dissipation mainly occurs inside the droplet due to the droplet's oscillatory motion. For small $Oh$, the problem is in the capillary-inertia regime and the oscillatory motion resulting from the coalescence and droplet-surface interaction persists with large amplitude for longer time because the viscous damping is relatively weak. For large $Oh$, the liquid viscosity damps the droplet's oscillation faster whereas the translational motion is not as much affected.

### S3.4 Comparison between different models

We have done some quantitative analyses for two sets of data (the experimental data in [3] and the simulation data in [20]) using the present model and the fitting function in [3]. Specifically, we calculated the average difference between the data on the jumping velocity (measured in experiments or simulation) and the prediction by the model or fitting function scaled by the maximum jumping velocity among the data, which can be written as $\Delta\tilde{V}^*_j = \frac{1}{V^*_{j,max}} \sqrt{\frac{1}{n_d} \sum_{i=1}^{n_d} (V^*_{j,i} - V^*_{j,i,m}(Oh_i))^2}$, where $n_d$ is the total number of data points, $V^*_{j,max}$

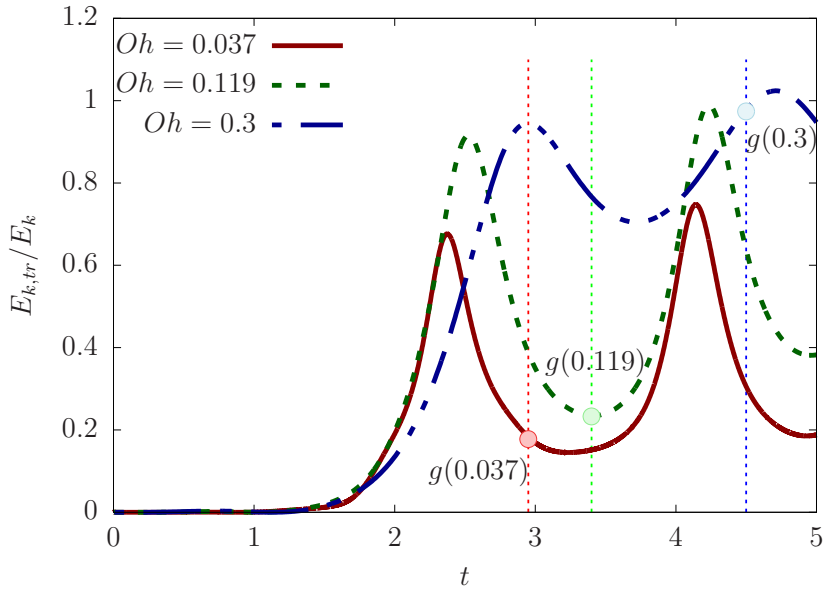


Figure S10: Evolution of the ratio between the translational kinetic energy and total kinetic energy of the droplet $1/(n+1)$ at three different $Oh$ numbers. The common parameters are $r_\rho = 50$, $r_\eta = 58.8$, and $\theta_w = 180°$. The three vertical dashed lines indicate the times for the droplet jumping $t_{jump}$ for the three cases (from left to right are $Oh = 0.037$, 0.119 and 0.3).

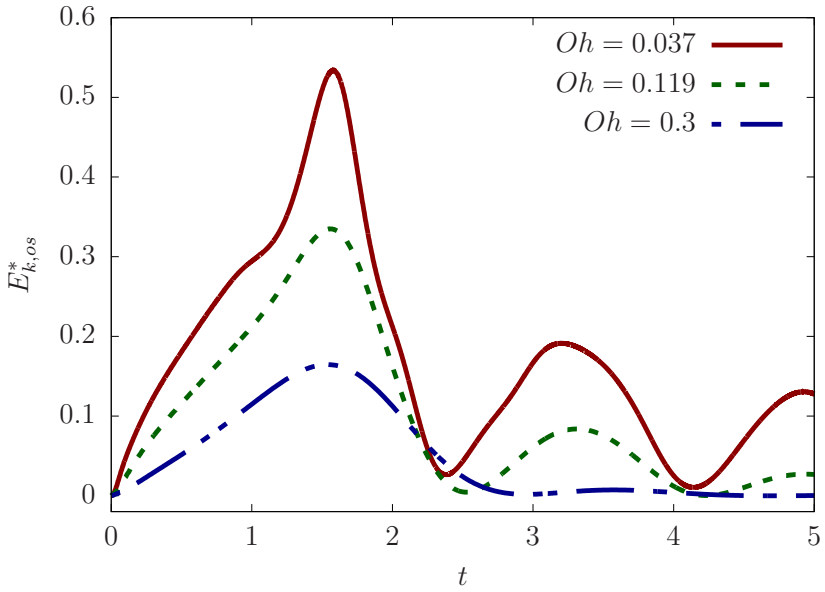


Figure S11: Evolution of the oscillatory kinetic energy of the droplet $E^*_{k,os}$ at three different $Oh$ numbers. The common parameters are $r_\rho = 50$, $r_\eta = 58.8$, and $\theta_w = 180°$.

is the maximum jumping velocity among the data set, $V^*_{j,i}$ and $Oh_i$ are the measured jumping velocity and $Oh$ number for the $i-$th data point, and $V^*_{j,i,m}(Oh_i)$ is the model prediction at $Oh_i$. When compared with the experimental data in [3], the relative differences $\Delta\tilde{V}^*_j$ for the present model and the fitting function in [3] are 14.3% and 13.8% respectively. Due to the significant scatting in the experiment data, both models have relatively large differences and they appear to have comparable prediction capability. When compared with the simulation data in [20], the relative differences $\Delta\tilde{V}^*_j$ for the present model and the fitting function in [3] are 4.7% and 27.7% respectively. The much larger difference in the fitting function of [3] is due to that it was obtained by fitting simulation data for the small $Oh$ regime ($Oh < 0.12$) while the data in [20] cover the large $Oh$ regime.

When compared with the fitting function in [3] which was based on direct fitting of their simulation data at $Oh < 0.12$, the present model involves more coefficients and looks more complicated and less straightforward to use. Nevertheless, the present model also has its own advantages. First, it employs simulation data at high $Oh$ numbers and deals with the low and high $Oh$ regimes separately. Thus, it can give better predictions for very small droplets with radii close to or smaller than $1\mu m$. Second, the present model provides more physical insights and information on the energy dissipation and the different components of the droplet's KE, making it easier to assess how different factors contribute to the reduction of energy conversion efficiency for a given case.

# S4 Modeling Coalescence-Induced Droplet Jumping on a Superhydrophobic Surface

## S4.1 Three different states and the area and volume calculations

Figure S12 shows the three states for the coalescence-induced droplet jumping on a superhydrophobic surface with an apparent contact angle $\theta_w$. To simplify the illustration, the nanostructures (if any) are hidden and the surface appears to be flat and homogenous in fig. S12. In State 1 (the initial state before coalescence), the two droplets both assume a shape on the substrate corresponding to the equilibrium state for $\theta_w$. In State 2 (the intermediate state after coalescence), the coalesced droplet on the substrate assumes the equilibrium state for $\theta_w$. In State 3 (the free state), the coalesced droplet assumes a spherical shape away from the surface. We use $\varphi_i$ and $r_{f,i}$ to denote the fraction of the projected surface area wetted by the droplet and the roughness ratio of the wet area in State $i$. The areas in States 1 are $A_{lg,1} = 2[\pi R^2(2-2\cos\theta_w) + (1-\varphi_1)(\pi R^2\sin^2\theta_w)]$, $A_{sl,1} = 2r_{f,1}\varphi_1(\pi R^2\sin^2\theta_w)$. The areas in States 2 are $A_{lg,2} = \pi R_m^2(2-2\cos\theta_w) + (1-\varphi_2)(\pi R_m^2\sin^2\theta_w)$, $A_{sl,2} = r_{f,2}\varphi_2(\pi R_m^2\sin^2\theta_w)$ where $R_m = 2^{\frac{1}{3}}R$ is the radius of the merged sessile droplet. The areas for State 3 are $A_{lg,3} = 4\pi R_f^2 (= A_f)$ and $A_{sl,3} = 0$ with $R_f = [3V_2/(4\pi)]^{\frac{1}{3}} = [(2-3\cos\theta_w+\cos^3\theta_w)/2]^{\frac{1}{3}}R$ being the radius

of the final free spherical droplet. In State $i$, one has the surface energy $E_{s,i} = \sigma A_{lg,i} + \sigma_{sl} A_{sl,i} + \sigma_{sg} A_{sg,i} = \sigma A_{lg,i} + (\sigma_{sl} - \sigma_{sg}) A_{sl,i} + \sigma_{sg} A_{tot} = \sigma A_{lg,i} - \sigma \cos\theta_Y A_{sl,i} + \sigma_{sg} A_{tot}$ where $A_{sg,i}$ is the area between the solid and gas phases in State $i$, Young's equation $\sigma_{sg} = \sigma_{sl} + \sigma \cos\theta_Y$ and $A_{tot} = A_{sl,i} + A_{sg,i}$ have been used. Substituting the expressions for various areas in States 1 and 2, one has [18] $\Delta E_{s,12} = \pi\sigma R^2[(2-2^{\frac{2}{3}})(2-2\cos\theta_w) - \sin^2\theta_w(2[\Phi(\varphi)]_1 - 2^{\frac{2}{3}}[\Phi(\varphi)]_2)]$ where $\Phi(\varphi) = r_f\varphi\cos\theta_Y + \varphi - 1$. Similarly, substituting the expressions for various areas in State 2 and 3, one gets $\Delta E_{s,23} = \pi\sigma R^2[2^{\frac{2}{3}}(2-2\cos\theta_w) - 2^{\frac{2}{3}}[\Phi(\varphi)]_2 \sin^2\theta_w - 4[(2-3\cos\theta_w + \cos^3\theta_w)/2]^{\frac{2}{3}}] = 2^{\frac{2}{3}}\pi\sigma R^2[(2-2\cos\theta_w) - [\Phi(\varphi)]_2 \sin^2\theta_w - 2^{\frac{2}{3}}(2-3\cos\theta_w + \cos^3\theta_w)^{\frac{2}{3}}]$. The volume of one droplet in State 1 is found to be $\Omega_0 = \frac{1}{3}\pi R^3(2-3\cos\theta_w + \cos^3\theta_w)$, and that of the merged sessile droplet in State 2 is $\Omega_{drop} = 2\Omega_0$.

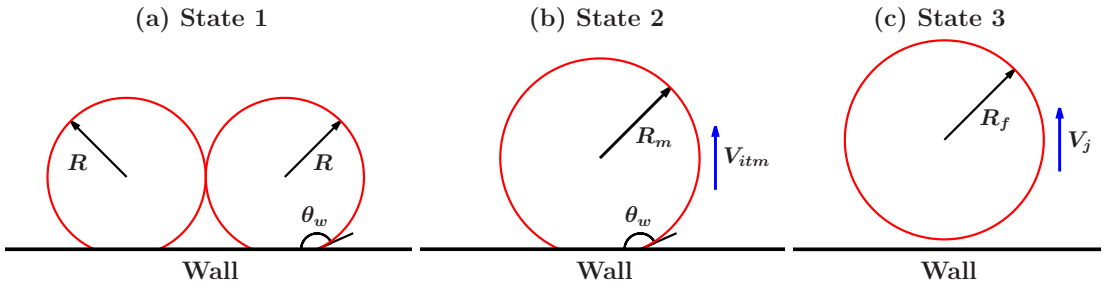


Figure S12: Three states in the coalescence-induced droplet jumping from a superhydrophobic surface.

## S4.2 On the work to overcome surface adhesion

First a flat and homogeneous surface ($\theta_Y = \theta_w$, $\varphi = 1$, $r_f = 1$) is examined. The areas in State 2 are simplified as $A_{lg,2} = 2^{\frac{2}{3}}\pi R^2(2-2\cos\theta_w)$, $A_{sl,2} = 2^{\frac{2}{3}}\pi R^2 \sin^2\theta_w$. Let us consider an "imaginary" state of the droplet with a flat bottom obtained by shifting the droplet in State 2 upwards from the wall without any shape changes (denoted as "State 3i", see fig. S13) and use $A_{cap}(= A_{lg,2} + A_{sl,2})$ to denote the surface area of the droplet in State 3i. The usual work to overcome the adhesion by the Young-Dupre equation $W_{23}$ is actually calculated from the energy change between State 2 and State 3i [17], i.e., $W_{23} = -\Delta E_{s,23i} = -(E_2 - E_{3i}) = -\sigma[A_{lg,2} - (A_{lg,2} + A_{sl,2}) - A_{sl,2}\cos\theta_w] = \sigma(1+\cos\theta_w)A_{sl,2} = (\sigma R^2)2^{\frac{2}{3}}\pi \sin^2\theta_w(1+\cos\theta_w)$. For sufficiently hydrophobic surfaces (e.g., $\theta_w > 120°$), it can be found that $\Delta E_{s,23} \approx -\frac{W_{23}}{2}$ (see fig. S14).

Next, we examine surfaces with nanostructures for which the Young-Dupre equation gives $W_{23} = \sigma(1+\cos\theta_Y)A_{sl,2}$ with $A_{sl,2} = r_f\varphi\pi 2^{\frac{2}{3}}R^2\sin^2\theta_w$. As the three surface parameters satisfy $r_f\varphi\cos\theta_Y + \varphi - 1 = \cos\theta_w$, only two of them can vary independently for a given apparent contact angle $\theta_w$. To assess their effects, we examine the dependence of the ratio $-\Delta E_{s,23}/W_{23}$ on the fraction of the projected solid surface area wetted by the droplet $\varphi$ for three different values of the roughness ratio $r_f$. Note that $-\Delta E_{s,23}/(\sigma R^2)$ is a positive constant for a given $\theta_w$. Figure S15a shows how the ratio $-\Delta E_{s,23}/W_{23}$ varies with $\varphi$ and fig. S15b shows how the

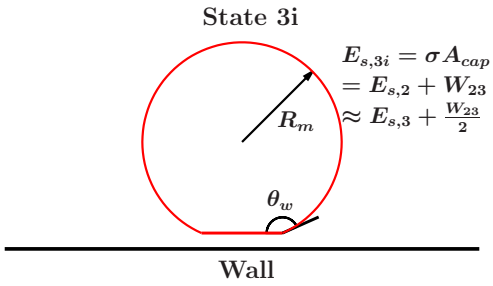


Figure S13: State 3i is an "imaginary" state obtained by shifting the droplet in State 2 upwards from the surface without any shape changes (as if it was a rigid body). The usual work to overcome surface adhesion is calculated according to the Young-Dupre equation as $W_{23} = E_{s,3i} - E_{s,2} = \sigma(1+\cos\theta_w)A_{sl,2} = \sigma(1+\cos\theta_w)(2^{\frac{2}{3}}\pi R^2 \sin^2\theta_w)$ (for a flat wall).

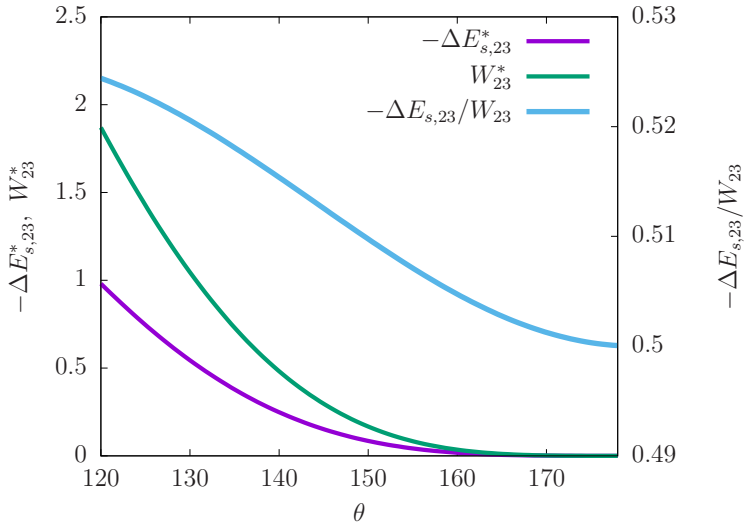


Figure S14: Variations of the dimensionless change in surface energy $-\Delta E^*_{s,23} = -\Delta E_{s,23}/(\sigma R^2)$, the dimensionless work to overcome surface adhesion $W^*_{23} = W_{23}/(\sigma R^2)$ and their ratio $-\Delta E_{s,23}/W_{23}$ with the wall contact angle $\theta_w$ (for a flat wall).

intrinsic contact angle $\theta_Y$ changes with $\varphi$ (dictated by the equation $r_f\varphi\cos\theta_Y+\varphi-1=\cos\theta_w$) at $r_f=1.0$, 1.1 and 1.2 with $\theta_w=155°$. It is seen that when $r_f=1.0$ the area fraction $\varphi$ does not affect $W_{23}$. In fact, when $r_f=1.0$, $W_{23}=\sigma(1+\cos\theta_Y)r_f\varphi\pi 2^{\frac{2}{3}}R^2\sin^2\theta_w=\sigma(1+\cos\theta_w)\pi 2^{\frac{2}{3}}R^2\sin^2\theta_w$ (i.e., same as that for a flat wall with $\theta_w$). When $r_f>1.0$, $W_{23}$ increases with $\varphi$ (because $-\Delta E_{s,23}/W_{23}$ decreases with $\varphi$), and $\varphi$ can affect $W_{23}$ significantly especially when $r_f$ is large.

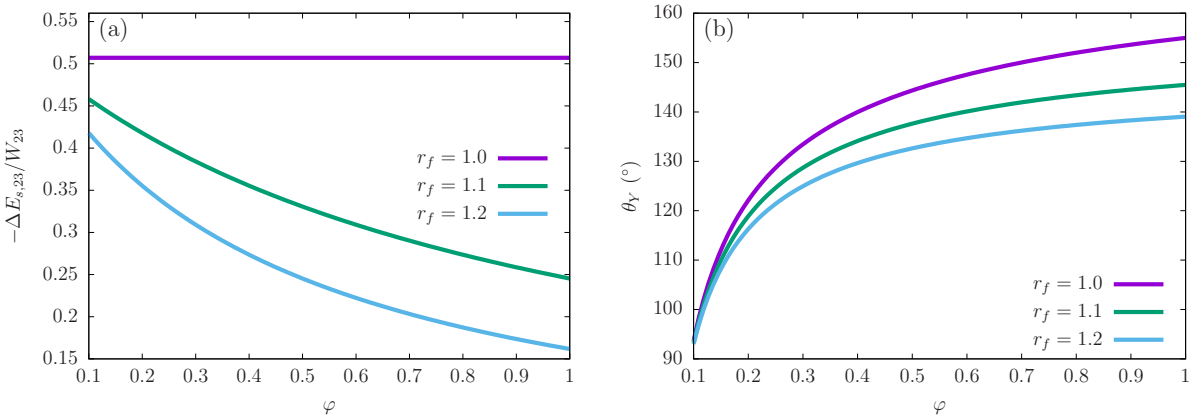


Figure S15: Variations of (a) the ratio $-\Delta E_{s,23}/W_{23}$ with the fraction of the projected solid surface area wetted by the droplet $\varphi$ (b) the intrinsic contact angle $\theta_Y$ with $\varphi$ at three different values of the roughness ratio of the wet area $r_f$ at State 2 while the apparent contact angle is fixed at $\theta_w=155°$.

In reality, when the droplet jumps off the surface, it is deformed due to the finite adhesion of the surface and deviates from a perfect sphere to some extent (e.g., see fig. 2 in [16]). Some analyses of the jumping stage (State 2 to 3) were also given in [12] (see fig. 7 therein and related discussions). The droplet shape at the jumping time could be better approximated by a prolate spheroid than by a perfect sphere. This state is denoted as "State 3a" (see fig. S16). For a prolate spheroid having a polar radius $R_c$ and an equatorial radius $R_a$ ($\leq R_c$), its volume is given by $V_{ps}=\frac{4}{3}\pi R_a^2R_c$ and it surface area is given by $A_{ps}=2\pi R_a^2+2\pi\frac{R_aR_c^2}{\sqrt{R_c^2-R_a^2}}\arcsin\frac{\sqrt{R_c^2-R_a^2}}{R_c}$ [21]. From volume conservation, one has $V_{ps}=\frac{4}{3}\pi R_a^2R_c=\frac{4}{3}\pi R_f^3$. By defining the ratio of the polar radius over the equatorial radius $k_{ca}=R_c/R_a$, one has $k_{ca}=(R_f/R_a)^3$ and $A_{ps}=2\pi R_f^2k_{ca}^{-\frac{2}{3}}(1+\frac{k_{ca}^2}{\sqrt{k_{ca}^2-1}}\arcsin\frac{\sqrt{k_{ca}^2-1}}{k_{ca}})$. Figure S17a shows the variation of the surface area of the prolate spheroid $A_{ps}$ with the radius ratio $k_{ca}$ when the wall contact angle is $\theta_w=155°$. It can be found that as $k_{ca}$ increases (the droplet is more stretched in the vertical direction), $A_{ps}$ increases (its minimum is achieved when $k_{ca}=1$). Figure S17b plots the variation of the difference between the surface energy of the prolate spheroid and that of the sphere scaled by $W_{23}$ (i.e., $\sigma(A_{ps}-A_f)/W_{23}$) with the radius ratio $k_{ca}$ at $\theta_w=155°$ (for a wall with $r_f=1.0$ and $W_{23}=\sigma(1+\cos\theta_w)\pi 2^{\frac{2}{3}}R^2\sin^2\theta_w$). In fig. S17b, the intersection point gives the value of $k_{ca}$ ($\approx 1.115$) at which the surface energy of the droplet in State 3a is equal to that at State 3i. As noted above, with the assumption that the droplet in State 3 is a perfect sphere, one finds that $\Delta E_{s,23}\approx-\frac{W_{23}}{2}$. When the droplet is stretched by the adhesion force during the jumping process to become a prolate spheroid with $k_{ca}\approx 1.115$, its surface energy is about $\frac{W_{23}}{2}$ higher than a perfect sphere and the surface energy change is $\Delta E_{s,23a}\approx-\frac{W_{23}}{2}-\frac{W_{23}}{2}=-W_{23}$. The

above gives a possible scenario that explains why the Young-Dupre equation (used for the jumping stage) can provide more accurate predictions.

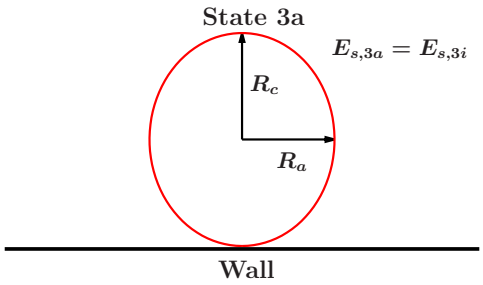


Figure S16: State 3a is closer to the actual situation (than a perfect sphere assumed in State 3) with the droplet stretched in the vertical direction by the adhesion force during the jumping stage and the droplet has the same surface energy as State 3i (about $W_{23}/2$ larger than the surface energy in State 3).

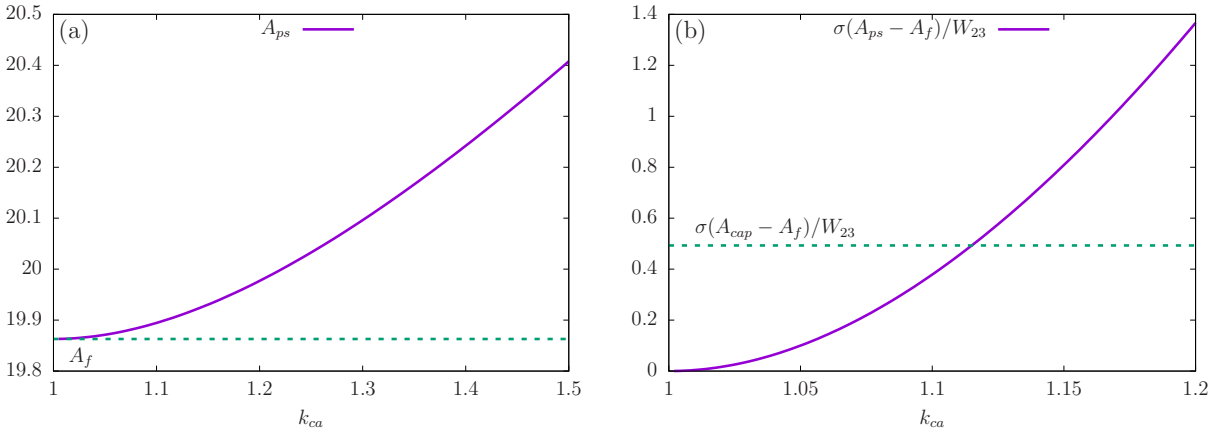


Figure S17: Variations of (a) the surface area of the prolate spheroid $A_{ps}$ scaled by $R^2$ (b) the difference between the surface energy of the prolate spheroid and that of the sphere scaled by $W_{23}$ with the radius ratio $k_{ca} = R_c/R_a$. The wall contact angle is $\theta_w = 155°$. The horizontal dashed line in (a) indicates the surface area of the perfect sphere $A_f$. The horizontal dashed line in (b) indicates the difference between with $\sigma A_{cap}$ and $\sigma A_f$ scaled by $W_{23}$.

## S4.3 On the model by Cha et al.

To simplify the comparison, the wall is assumed to be flat and the required areas in different states are $A_{lg,1} = 2\pi R^2(2 - 2\cos\theta_w)$, $A_{sl,1} = 2\pi R^2 \sin^2\theta_w$, $A_{sl,2} = \pi 2^{\frac{2}{3}} R^2 \sin^2\theta_w$, and $A_{lg,3} = 4\pi R_f^2$. Written in the present symbols, the model in [1] gives the jumping velocity through the following equation,

$$\frac{1}{2}\rho_L \Omega_{drop} V_j^2 = \eta_j[\sigma(A_{lg,1} - A_{lg,3}) + \sigma(1 + \cos\theta_w)(A_{sl,2} - A_{sl,1})] - \sigma(1 + \cos\theta_w)A_{sl,2}, \tag{S4.1}$$

where $\eta_j$ is the energy conversion efficiency on a nonwetting surface given by $\eta_j = \eta_{inv}[e^{-bOh} - (1 - e^{-bOh})e^{-bOh_c}]$ for $Oh \leq Oh_c$ ($\eta_{inv} \approx 0.064$ is the maximum efficiency in the inviscid limit, $Oh_c \approx 0.33$ is their estimated critical

$Oh$ number, and $b = 10.165$ is a fit parameter). More details may be found in eqs. (1-16) in [1] . The released surface energy in the first stage (the terms in the square brackets of eq. (S4.1)) is found to be, $\sigma(A_{lg,1} - A_{lg,3}) + \sigma(1+\cos\theta_w)(A_{sl,2} - A_{sl,1}) = \sigma R^2\pi\{4[(1-\cos\theta_w) - ((2-3\cos\theta_w+\cos^3\theta_w)/2)^{\frac{2}{3}}] + (1+\cos\theta_w)\sin^2\theta_w(2^{\frac{2}{3}}-2)\}$.

# References


[1] Hyeongyun Cha, Chenyu Xu, Jesus Sotelo, Jae Min Chun, Yukihiro Yokoyama, Ryan Enright, and Nenad Miljkovic. Coalescence-induced nanodroplet jumping. *Physical Review Fluids*, 1(064102), 2016.

[2] Shiyi Chen and Gary D. Doolen. Lattice Boltzmann method for fluid flows. *Annu. Rev. Fluid Mech.*, 30: 329, 1998.

[3] Ryan Enright, Nenad Miljkovic, James Sprittles, Kevin Nolan, Robert Mitchell, and Evelyn N. Wang. How coalescing droplets jump. *ACS Nano*, 8(10):10352–10362, 2014.

[4] Abbas Fakhari, Diogo Bolster, and Li-Shi Luo. A weighted multiple-relaxation-time lattice Boltzmann method for multiphase flows and its application to partial coalescence cascades. *J. Comput. Phys.*, 2017.

[5] Samaneh Farokhirad, Jeffrey M. Morris, and Taehun Lee. Coalescence-induced jumping of droplet: Inertia and viscosity effects. *Phys. Fluids*, 27:102101, 2015.

[6] Jun-Jie Huang, Haibo Huang, Chang Shu, Yong Tian Chew, and Shi-Long Wang. Hybrid multiple-relaxation-time lattice-Boltzmann finite-difference method for axisymmetric multiphase flows. *Journal of Physics A: Mathematical and Theoretical*, 46(5):055501, 2013.

[7] Jun-Jie Huang, Jie Wu, and Haibo Huang. An alternative method to implement contact angle boundary condition and its application in hybrid lattice-boltzmann finite-difference simulations of two-phase flows with immersed surfaces. *Eur. Phys. J. E*, 41:17, 2018.

[8] David Jacqmin. Calculation of two-phase Navier-Stokes flows using phase-field modeling. *J. Comput. Phys.*, 155:96–127, 1999.

[9] Pierre Lallemand and Li-Shi Luo. Theory of the lattice Boltzmann method: Dispersion, dissipation, isotropy, Galilean invariance, and stability. *Phys. Rev. E*, 61:6546, 2000.

[10] Taehun Lee. Effects of incompressibility on the elimination of parasitic currents in the lattice boltzmann equation method for binary fluids. *Comput. Math. Appl.*, 58:987–994, 2009.

[11] Taehun Lee and Lin Liu. Lattice Boltzmann simulations of micron-scale drop impact on dry surfaces. *J. Comput. Phys.*, 229:8045–8063, 2010.

[12] Hongxia Li, Weilin Yang, Abulimiti Aili, and TieJun Zhang. Insights into the impact of surface hydrophobicity on droplet coalescence and jumping dynamics. *Langmuir*, 33:8574–8581, 2017.

[13] Fangjie Liu, Giovanni Ghigliotti, James J. Feng, and Chuan-Hua Chen. Numerical simulations of self-propelled jumping upon drop coalescence on non-wetting surfaces. *J. Fluid Mech.*, 752:39–65, 2014.

[14] Cunjing Lv, Pengfei Hao, Zhaohui Yao, Yu Song, Xiwen Zhang, and Feng He. Condensation and jumping relay of droplets on lotus leaf. *Appl. Phys. Lett.*, 103(2), 2013.

[15] Youngsuk Nam, Hyunsik Kim, and Seungwon Shin. Energy and hydrodynamic analyses of coalescence-induced jumping droplets. *Appl. Phys. Lett.*, 103:161601, 2013.

[16] Youngsuk Nam, Donghyun Seo, Choongyeop Lee, and Seungwon Shin. Droplet coalescence on water repellant surfaces. *Soft Matter*, 11(1):154–160, 2015.

[17] Malcolm E. Schrader. Young-Dupre revisited. *Langmuir*, 11(9):3585–3589, 1995.

[18] Feng Chao Wang, Fuqian Yang, and Ya Pu Zhao. Size effect on the coalescence-induced self-propelled droplet. *Appl. Phys. Lett.*, 98(5):2011–2014, 2011.

[19] Xiao-Ping Wang, Tiezheng Qian, and Ping Sheng. Moving contact line on chemically patterned surfaces. *J. Fluid Mech.*, 605:59–78, 2008.

[20] Joram Wasserfall, Patric Figueiredo, Reinhold Kneer, Wilko Rohlfs, and Philipp Pischke. Coalescence-induced droplet jumping on superhydrophobic surfaces: Effects of droplet mismatch. *Physical Review Fluids*, 2(12):1–17, 2017.

[21] Eric W. Weisstein. Prolate spheroid. http://mathworld.wolfram.com/ProlateSpheroid.html.

[22] Pengtao Yue, Chunfeng Zhou, and James J. Feng. Sharp-interface limit of the Cahn-Hilliard model for moving contact lines. *J. Fluid Mech.*, 645:279–294, 2010.